arXiv:1601.03474v1 [stat.AP] 14 Jan 2016

A Unified Statistical Approach to Modeling the Shape of Human Hyoid Bones in CT Images

Moo K. Chung[1,2,3], Nagesh Adluru[3], Houri K. Vorperian[2]
[1]Department of Biostatistics and Medical Informatics
[2]Vocal Tract Laboratory, Waisman Center
[3]Waisman Laboratory for Brain Imaging and Behavior
University of Wisconsin-Madison, USA
mkchung@wisc.edu

January 15, 2016

Abstract

We present a unified statistical approach to modeling 3D anatomical objects extracted from medical images. Due to image acquisition and preprocessing noises, it is expected the imaging data is noisy. Using the Laplace-Beltrami (LB) eigenfunctions, we smooth out noisy data and perform statistical analysis. The method is applied in characterizing the 3D growth pattern of human hyoid bone between ages 0 and 20 obtained from computed tomography (CT). We detected a significant age effect on localized parts of the hyoid bone.

1 Introduction

For normally developing children, age and gender could be major factors that affect the functions and structures of growing hyoid bone. As in other developmental studies [13, 32], we expect highly localized complex growth pattern to emerge between ages 0 and 20 in the hyoid bone. It is expected the growth to be outward with respect to the surface of the bone. However, it is unclear what specific parts of the hyoid bone are growing. This provides a biological motivation for a need to develop a local surface-based morphometric technique beyond simple volumetric techniques that cannot detect localized subtle anatomical changes along the hyoid bone surface.

The end results of existing surface-based morphometric studies in medical imaging are statistical parametric maps (SPM) that shows statistical

significance of growth at each surface mesh vertex [13, 27, 39]. In order to obtain stable and robust SPM, various signal smoothing and filtering methods have been proposed. Among them, diffusion equations, kernel smoothing, and wavelet-based approaches are probably most popular. Diffusion equations have been widely used in image processing as a form of noise reduction starting with Perona and Malik in 1990's [25]. Although numerous techniques have been developed for performing diffusion along surfaces [12, 2, 29, 28, 22, 30], most approaches are nonparametric and requires finite element or finite difference schemes which are known to suffer various numerical instabilities [11].

Kernel smoothing based models have been also proposed for surface and manifolds data [6, 11]. The kernel methods basically smooth data as weighted average of neighboring mesh vertices using mostly a Gaussian kernel and its iterative application is supposed to approximates the diffusion process. Recently, wavelets have been popularized for surface and graph data. Spherical wavelets have been used on brain surface data that has been mapped onto a sphere [23, 7]. Since wavelet basis functions have local supports in both space and scale, the wavelet coefficients from the scale-space decomposition using the spherical wavelets provides shape features that describe local shape variation at a variety of scales and spatial locations. However, spherical wavelets have an intrinsic problem that they require to establish a smooth mapping from the surface to a unit sphere, which introduces a serious metric distortion. The spherical mapping such as conformal mapping introduces serious metric distortion which usually compounds SPM. Furthermore, such basis functions defined on sphere seem to be suboptimal rather than those directly defined on anatomical surface, in detecting locations or scales of shape variations. To remedy the limitation of spherical wavelets, spectral graph wavelet transform defined on a graph has been applied to arbitrary surface meshes by treating surface meshes as graphs [3, 17, 19]. Wavelet transform is a powerful tool decomposing a signal or function into a collection of components localized at both location and scale. Although all three methods (diffusion-, kernel- and wavelet-based) look different from each other, it is possible to develop a unified framework that relates all of them in a coherent statistical fashion.

Starting with a symmetric positive definite kernel, we propose a novel unified kernel regression framework within the Hilbert space theory. The proposed kernel regression works for any symmetric positive definite kernel, which behaves like weights between two functional data. We show how this facilitates a coherent statistical inference for functional signals defined on an arbitrary manifold. The outline of this paper is as follows. (i) First, we

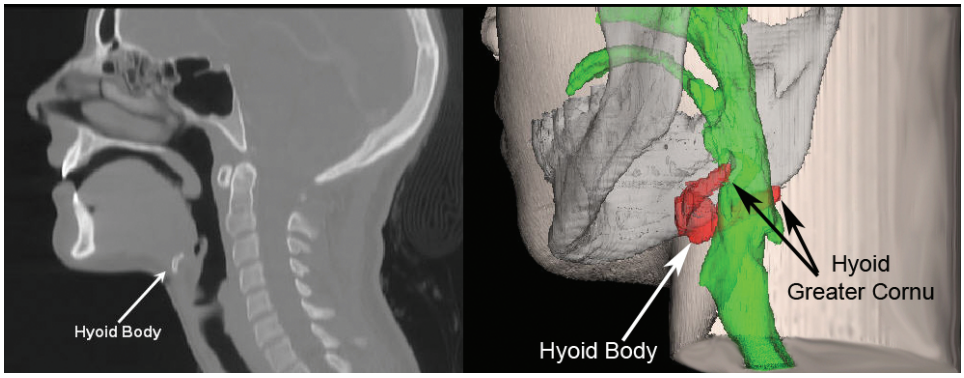

Figure 1: CT image showing the location of the hyoid bone and 3D model showing the relative location of the hyoid bone with respect to the mandible (gray) and vocal tract structures (green).

present a unified bivariate kernel regression that is related to diffusion-like equations. (ii) We establish the relationship between the kernel regression and recently popular spectral graph wavelets for manifolds. The proposed kernel regression is shown to be equivalent to the wavelet coefficients. This mathematical equivalence levitates a need for constructing wavelets using a complicated computational machinery as often done in previous diffusion wavelet constructions [3, 17, 19]. (iii) A unified statistical inference framework is developed for neuroimaging applications by linking the kernel regression to the random field theory [31, 38]. (iv) Subsequently, we illustrate how the kernel regression procedure can be used to localize the hyoid bone growth pattern in human.

2 Preliminary

First, let us illustrate two statistical problems in an Euclidean space that motivate the development of the proposed kernel regression in manifolds. Consider measurements f_i sampled at $p_i \in \mathbb{R}^d$. The measurements are usually modeled as

$$f_i = h(p_i) + \epsilon_i$$

with some noise ϵ_i and unknown mean function h that has to be estimated. In the well known local polynomial or kernel regression frameworks [6, 15, 24], a univariate kernel $G(p)$ is introduced to minimize the weighted least

squares of the form

$$\widehat{h}(p) = \arg\min_{\beta_0 \cdots \beta_k} \sum_{i=1}^{n} G(p - p_i) \Big| f_i - \sum_{j=0}^{k} \beta_j (p - p_i)^j \Big|^2. \tag{1}$$

Often Gaussian kernels are used for G. In many related local polynomial or kernel regression frameworks, kernel G and polynomial basis p^j are translated by the amount of p_i in fitting the data locally. In this fashion, at each data point p_i, exactly the same shape of kernel and distance are used. However, one immediately encounters a difficulty of directly generalizing the Euclidean formulation (1) to an arbitrary surface since it is unclear how to translate the kernel and basis in a coherent fashion.

A similar problem is also encountered in wavelets in a Euclidean space. Consider a wavelet basis $W_{t,q}(p)$ obtained from a mother wavelet W with scale and translation parameters t and q:

$$W_{t,q}(p) = \frac{1}{t} W\big(\frac{p - q}{t}\big). \tag{2}$$

Scaling a function on a surface is trivial. But the difficulty arises when one tries to define a mother wavelet and translate it on a surface. It is not straightforward to generalize the Euclidean formulation (2) to an arbitrary manifold. To remedy these two different but related problems, we propose to use a bivariate kernel and bypass the problem of translating a univariate kernel. By simply changing the second argument, it has the effect of translating the kernel.

3 Methods

In many anatomical studies in CT, measurements are sampled densely at the resolution 0.5mm or less so it is more practical to model the measurements as functions. Consider a functional measurement f defined on a manifold $\mathcal{M} \subset \mathbb{R}^d$. We assume the following additive model:

$$f(p) = h(p) + \epsilon(p), \tag{3}$$

where h is the unknown signal and ϵ is a zero-mean random field, possibly Gaussian. The manifold $\mathcal{M}$ can be a single connected or multiple disjoint components as our hyoid bone application. We further assume $f \in L^2(\mathcal{M})$, the space of square integrable functions on $\mathcal{M}$ with the inner product

$$\langle f, g \rangle = \int_{\mathcal{M}} f(p) g(p) \, d\mu(p),$$

where μ is the Lebesgue measure. Define a self-adjoint operator $\mathcal{L}$ satisfying

$$\langle g_1, \mathcal{L} g_2 \rangle = \langle \mathcal{L} g_1, g_2 \rangle$$

for all $g_1, g_2 \in L^2(\mathcal{M})$. Then $\mathcal{L}$ induces the eigenvalues λ_j and eigenfunctions ψ_j on $\mathcal{M}$:

$$\mathcal{L}\psi_j = \lambda_j \psi_j. \tag{4}$$

Without loss of generality, we can order the eigenvalues $0 = \lambda_0 \leq \lambda_1 \leq \lambda_2 \leq \cdots$. The eigenfunctions ψ_j form an orthonormal basis in $L^2(\mathcal{M})$. Then from Mercer's theorem [14], any smooth symmetric positive definite kernel on manifold $\mathcal{M}$ can be written as

$$K(p, q) = \sum_{j=0}^{\infty} \tau_j \psi_j(p) \psi_j(q) \tag{5}$$

for some τ_j. The constants τ_j are identified as follows. Apply the kernel convolution on the eigenfunction ψ_j:

$$K * \psi_j(p) = \int_{\mathcal{M}} K(p, q) \psi_j(q) \, d\mu(q). \tag{6}$$

Substituting (5) into (6), we have $K * \psi_j(p) = \tau_j \psi_j(p)$ indicating τ_j and ψ_j must be the eigenvalues and eigenfunctions of the convolution (6). However, the relationship between the two different sets of eigenvalues λ_j and τ_j is not yet given but will be shown shortly afterward.

3.1 Proposed kernel regression

Consider subspace $\mathcal{H}_k \subset L^2(\mathcal{M})$ spanned by the orthonormal basis $\{\psi_j\}$, i.e.

$$\mathcal{H}_k = \{\sum_{j=0}^{k} \beta_j \psi_j(p) : \beta_j \in \mathbb{R}\}.$$

We estimate h by minimizing the weighted distance to the space $\mathcal{H}_k$:

$$\widehat{h}(p) = \arg\min_{h \in \mathcal{H}_k} \int_{\mathcal{M}} \int_{\mathcal{M}} K(p, q) \Big| f(q) - h(p) \Big|^2 \, d\mu(q) \, d\mu(p). \tag{7}$$

Without loss of generality, we will assume the kernel to be a probability distribution so that

$$\int_{\mathcal{M}} K(p, q) \, d\mu(q) = 1$$

for all $p \in \mathcal{M}$. The solution of (7) has the following analytic expression:

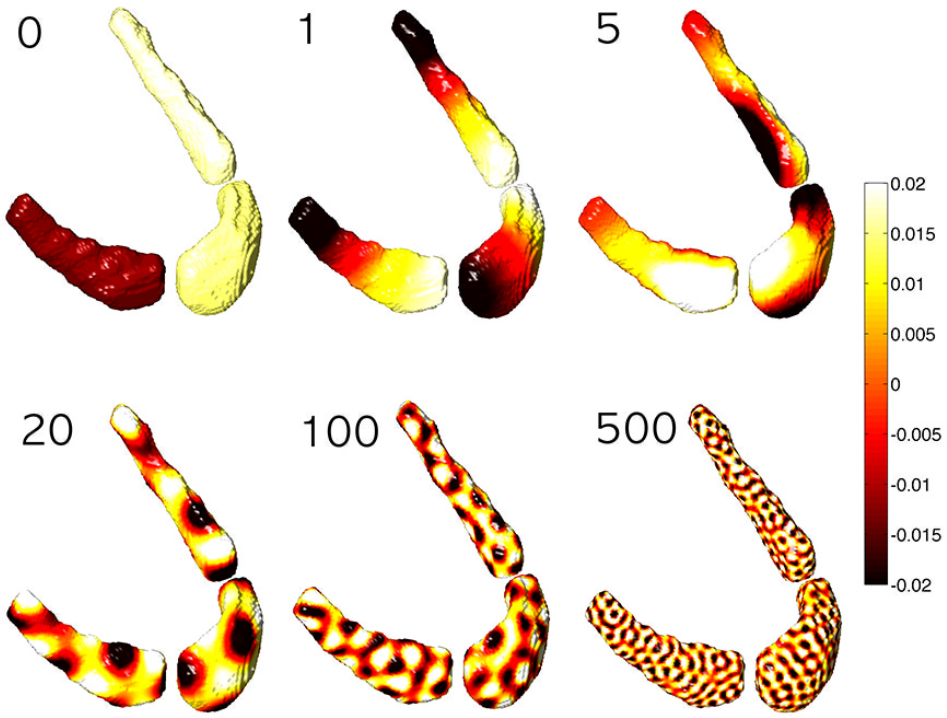

Figure 2: Laplace-Beltrami eigenfunctions ψ_j of various degrees ($j = 0, 1, 5, 20, 100, 500$) on the template. The first eigenfunction is constant in each component. As the degree increases, the spatial frequency increases.

Theorem 1.

$$\widehat{h}(p) = \arg\min_{h \in \mathcal{H}_k} \int_{\mathcal{M}} \int_{\mathcal{M}} K(p,q) \Big| f(q) - h(p) \Big|^2 \, d\mu(q) \, d\mu(p) = \sum_{j=0}^{k} \tau_j f_j \psi_j,$$

where $f_j = \langle f, \psi_j \rangle$ *are Fourier coefficients.*

Proof. See the Appendix. Theorem 1 generalizes the spherical regression on a unit sphere to an arbitrary manifold [9]. Theorem 1 implies that the kernel regression can be performed by simply computing the Fourier coefficients $f_j = \langle f, \psi_j \rangle$ without doing any numerical optimization. The numerically difficult optimization problem is reduced to the problem of computing Fourier coefficients. If the kernel K is a Dirac-delta function, the kernel regression simply collapses to the least squares estimation (LSE) which results in the

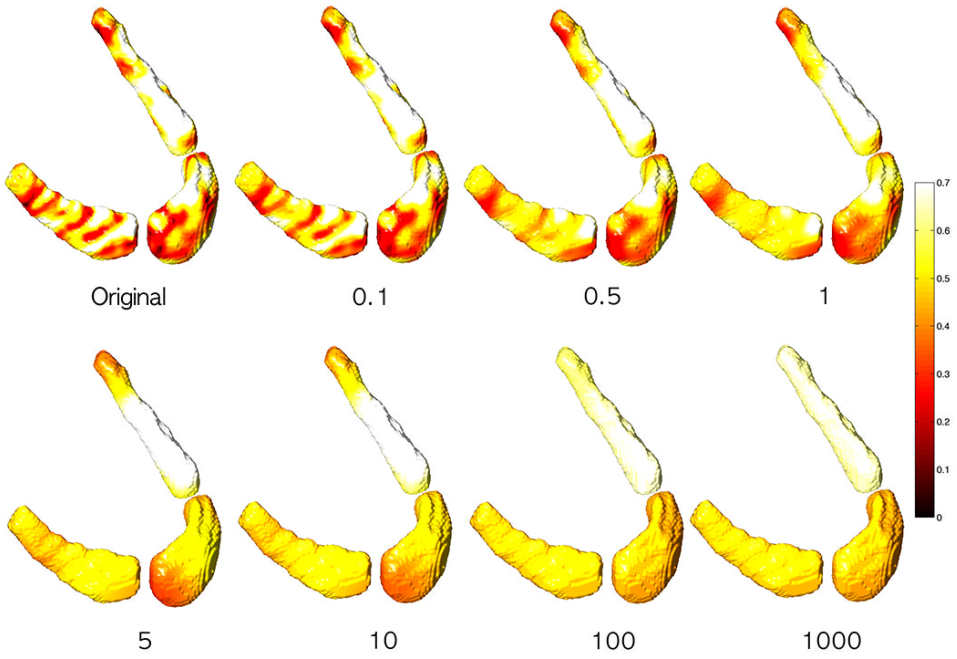

Figure 3: Heat kernel regression with different bandwidth between 0.1 and 1000. As the bandwidth increases, the kernel regression becomes inversely proportional to the square root of the surface area.

standard Fourier series, i.e.

$$\widehat{h}(p) = \arg\min_{h \in \mathcal{H}_k} \int_{\mathcal{M}} \left| f(q) - h(q) \right|^2 d\mu(q) = \sum_{j=0}^{k} f_j \psi_j.$$

It can be also shown that as $k \to \infty$, the kernel regression

$$\widehat{h} = \sum_{j=0}^{k} \tau_j f_j \psi_j$$

converges to convolution $K * f$ establishing the connection to the manifold-based kernel smoothing framework [5, 11]. Hence, asymptotically the proposed kernel regression should inherit many statistical properties of kernel smoothing.

3.2 Properties

The kernel regression can be shown to be related to the following diffusion-like Cauchy problem.

Theorem 2. *For an arbitrary self-adjoint differential operator $\mathcal{L}$, the unique solution of the following initial value problem*

$$\frac{\partial g(p,t)}{\partial t} + \mathcal{L}g(p,t) = 0, g(p,t=0) = f(p) \tag{8}$$

is given by

$$g(p,t) = \sum_{j=0}^{\infty} e^{-\lambda_j t} f_j \psi_j(p). \tag{9}$$

Proof. See the Appendix. For a particular choice of kernel K with $\tau_j = e^{-\lambda_j t}$, the proposed kernel regression $\widehat{h} = \sum_{j=0}^{k} \tau_j f_j \psi_j$ should converge to the solution of the diffusion-like equation. If we let $\mathcal{L}$ be the Laplace-Beltrami operator, (8) becomes an isotropic diffusion equation as a special case and we are then dealing with heat kernel

$$H_t(p,q) = \sum_{j=0}^{\infty} e^{-\lambda_j t} \psi_j(p) \psi_j(q),$$

which is often explored mathematical objects in various fields [5, 11].

In order to construct wavelets on an arbitrary graph and mesh, diffusion wavelet transform has been proposed recently [3, 17, 19]. The diffusion wavelet construction has been fairly involving so far. However, it can be shown to be a special case of the proposed kernel regression and the proposed method is substantially simpler to construct. Following the notations in [3, 17, 19], diffusion wavelet $W_{t,p}(p)$ at position p and scale t is given by

$$W_{t,q}(p) = \sum_{j=0}^{k} g(\lambda_j t) \psi_j(p) \psi_j(q),$$

for some scale function g. If we let $\tau_j = g(\lambda_j t)$, the diffusion wavelet transform is given by

$$\langle W_{t,p}, f \rangle = \int_{\mathcal{M}} W_{t,q}(p) f(p) \, d\mu(p) = \sum_{j=0}^{k} \tau_j f_j \psi_j(q),$$

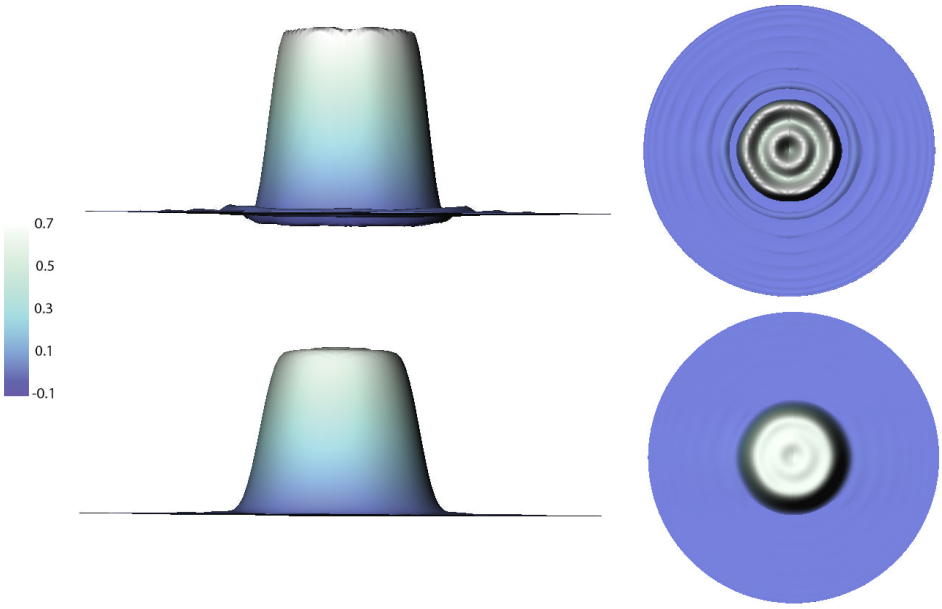

Figure 4: The Gibbs phenomenon on a hat shaped simulated surface showing the ringing effect on the traditional Fourier series expansion (top) and the reduced effect on the heat kernel regression (bottom). 7225 basis functions were used for the both cases and the bandwidth $t = 0.001$ is used for the kernel regression.

which is the exactly kernel regression we introduced. Hence, the diffusion wavelet transform can be simply obtained by doing the kernel regression without an additional wavelet machinery [19]. Further, if we let $g(\lambda_j t) = e^{-\lambda_j t}$, we have

$$W_{t,p}(q) = H_t(p, q),$$

which is a heat kernel. The bandwidth t of heat kernel controls resolution while the translation is done by shifting one argument in the kernel.

Although the kernel regression is constructed using global basis functions ψ_j, the kernel regression at each point p coincides with the diffusion wavelet transform at that point. Hence, just like wavelets, the kernel regression will have the localization property of wavelets. This is demonstrated in a toy example in Figure 4 with a hat-shaped surface in 3D. The hat-shaped step function is simulated as $z = 1$ for $x^2 + y^2 < 1$ and $z = 0$ for $1 \leq x^2 + y^2 \leq 2$. Then the step function is reconstructed using the Fourier series expansion via LSE (top) and kernel regression (bottom). In the both cases, up to 7225 basis functions were used. For the kernel regression, the heat kernel with bandwidth $t = 0.0001$ is used. LSE clearly shows the visible Gibbs

phenomenon, i.e., ringing artifact [8, 16] compared to the kernel regression.

3.3 Numerical Implementation

The Laplace-Beltrami operator is chosen as the self-adjoint operators $\mathcal{L}$ of choice. The eigenfunctions of the Laplace-Beltrami operator on an arbitrary curved surface is analytically unknown. So it is necessary to discretize (4) using the Cotan formulation as a generalized eigenvalue problem [41, 26]:

$$\mathbf{C}\psi = \lambda \mathbf{A}\boldsymbol{\psi}, \tag{10}$$

where $\mathbf{C}$ is the stiffness matrix, $\mathbf{A}$ is the mass matrix and $\boldsymbol{\psi} = (\psi(p_1), \cdots, \psi(p_n))'$ is the eigenfunction evaluated at n mesh vertices. Once we obtained the basis functions ψ_j, the corresponding Fourier coefficients β_j are estimated as

$$\beta_j = \mathbf{f}'\mathbf{A}\boldsymbol{\psi}_j,$$

where $\mathbf{f} = (f(p_1), \cdots, f(p_n))'$ and $\boldsymbol{\psi}_j = (\psi_j(p_1), \cdots, \psi_j(p_n))'$ [41]. Figure 2 shows few representative LB-eigenfunctions on the hyoid surface. For heat kernel regression, we used the bandwidth $\sigma = 5$ and 500 LB-eigenfunctions on the final template. The number of eigenfunctions used is more than sufficient to guarantee relative error less than 0.3% in our data.

3.4 Statistical Inference

We are interested in determining the significance of functional signals on a manifold 7. We borrow the statistical parametric mapping (SPM) framework for analyzing and visualizing statistical tests performed on the template surface that is often used in brain image analysis [2, 20, 33, 34, 40]. Since test statistics are constructed over all mesh vertices on the surface, multiple comparisons need to be accounted. For continuous functional data, the random field theory [31, 34, 38] is natural to use. The random field theory assumes the measurements to be smooth Gaussian random field. Heat kernel regression will make the data more smooth and Gaussian as well as increase the signal-to-noise ratio [10].

Consider a functional measurements $f_1, \cdots, f_n$ on manifold $\mathcal{M}$. In the simplest statistical setting, the measurements can be modeled as

$$f_i(p) = h(p) + \epsilon_i(p),$$

where h is an unknown group level signal and ϵ_i is a zero-mean Gaussian random field [38]. At each fixed point p, we are assuming $\epsilon_i \sim N(0, \sigma^2)$.

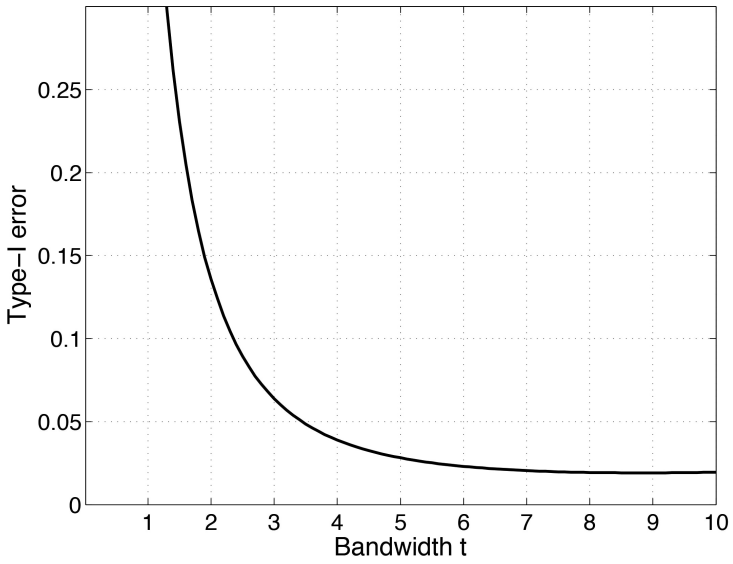

Figure 5: Type-I error plot over bandwidth t of kernel regression for testing the difference between the groups I and III. As the bandwidth increases, the multiple comparisons corrected type-I error decreases. The bandwidth 5 is chosen for the study. The choice of the bandwidth around 5 does not change the over-all Type-I error much.

We are interested in determining the significance of h, i.e.

$$H_0 : h(p) = 0 \text{ for all } p \in \mathcal{M} \quad \text{vs.} \quad H_1 : h(p) > 0 \text{ for some } x \in \mathcal{M}. \tag{11}$$

Note that any point p_0 that gives $h(p_0) > 0$ is considered as signal. The hypothsis (11) is an infinite dimensional multiple comparisons problem for continuously indexed hypotheses over the manifold $\mathcal{M}$. The underlying group level signal h is estimated using the proposed heat kernel regression. Subsequently, a test statistic is given by a T-field $T(p)$ or a F-field, which is simply given by the square of the T-field [38, 34].

For sufficiently high threshold z, the corrected type-I error of testing hypothesis (11) is given by

$$P\Big(\sup_{p\in\mathcal{M}} T(p) > z\Big) = \sum_{j=0}^{d} \mu_j(\mathcal{M})\rho_j(z),$$

where $\mu_d(\mathcal{M})$ is the j-th Minkowski functional or intrinsic volume of $\mathcal{M}$ and ρ_j is the j-th Euler characteristic (EC) density of T-field. Since the hyoid

bone is compact with no boundary but has three disconnected components, the Minkowski functionals are simply

$$\begin{aligned}\mu_2(\mathcal{M}) &= \text{area}(\mathcal{M})/2\\ \mu_1(\mathcal{M}) &= 0\\ \mu_0(\mathcal{M}) &= \chi(\mathcal{M}) = 3\times 2.\end{aligned}$$

The term μ_1 is zero since there is no boundary and μ_0 is simply the Euler characteristic of the template surface. Note that the Euler characteristic of a closed surface with no hole or handle is 2 and there are three such surfaces. The EC-densities of the T-field with ν degrees of freedom is given by

$$\begin{aligned}\rho_0(z) &= 1 - P(T_\nu \le z),\\ \rho_1(z) &= \frac{1}{\sqrt{2t^2}}\cdot\frac{1}{2\pi}\Big(1+\frac{z^2}{\nu}\Big)^{-(\nu-1)/2},\\ \rho_2(z) &= \frac{1}{2t^2}\cdot\frac{1}{(2\pi)^{3/2}}\frac{\Gamma(\frac{\nu+1}{2})}{(\frac{\nu}{2})^{1/2}\Gamma(\frac{\nu}{2})}z\Big(1+\frac{z^2}{\nu}\Big)^{-(\nu-1)/2}.\end{aligned}$$

The EC-density of the F-field is similarly given in [38, 31]. The EC-density has the kernel bandwidth $2t^2$ in the formulation so the inference is done at a particular smoothing scale. Figure 5 shows the type-I error plot over different bandwidth t of the kernel regression in our application. As the bandwidth t becomes zero, the type-I error increases. When $t = 0$, the kernel regression collapse to the usual Fourier series expansion. Note that the Fourier expansion with 500 LB-eigenfunctions is close to the original data without any smoothing. Hence, the proposed kernel regression can be viewed as having substantially smaller type-I error compared to the Fourier series expansion as well as the original data demonstrating a better statistical performance.

Type-II error and the statistical power can be also computed similarly.

Theorem 3. *The statistical power $\mathcal{P}$ of testing the hypotheses*

$$H_0 : h(p) = 0 \ \text{ for all } p \in \mathcal{M} \ \text{ vs. } \ H_1 : h(p) = c\sigma > 0 \ \text{ for some } p \in \mathcal{M}.$$

using the T random field $T(p)$ is given by

$$\mathcal{P}(n) \approx 1 - \exp\Big[-\sum_{j=0}^{d}\mu_j(\mathcal{M}_1)\rho_j(t^*_\alpha - c\sqrt{n})\Big],$$

where t^*_α is the α-quantile given by

$$\alpha = P\Big(\sup_{p\in\mathcal{M}} T(p) > t^*_\alpha\Big).$$

Proof. See the Appendix.

4 Application

4.1 CT Imaging Data and Preprocessing

The study consists of high resolution CT images of 70 normal subjects ages between 0 and 20 years (mean age = 58.0 $\pm$ 11.3 years). CT scans were converted to DICOM format and Analyze 8.1 software package (AnalyzeDirect, Inc., Overland Park, KS) was then used in segmenting binary hyoid bone images by a trained individual rater in the native space by simple image intensity thresholding and careful manual editing. A nonlinear image registration using the diffeomorphic shape and intensity averaging technique with cross-correlation as similarity metric was performed through Advanced Normalization Tools (ANTS) [4]. A study-specific template was constructed. We have chosen a 12 year old subject identified as F155 as the initial template and aligned the remaining 69 hyoids to the initial template affinely to remove the overall size variability. Some subject may have larger hyoid than others so it is necessary to remove the global size differences in local shape modeling. From the affine transformed individual hyoid surfaces, we performed the diffeomorphic nonlinear image registration to the template using ANTS.

Then by averaging the inverse deformation fields from the initial template to individual hyoid, we obtain the yet another final template. Figure 6 shows the initial and final templates. The isosurface of the final template volume is extracted using the marching cube algorithm [21]. Figure 7 shows the mean displacement differences between the groups I and II (top) and II and III (bottom). Each row shows the group differences of the displacement: group II - group I (first row) and group III - group II (second row). The arrows are the growth direction given by the mean displacement differences and colors indicate their lengths in mm. We are interested in localizing the regions of hyoid bone growth between the age groups.

70 subjects are binned into three age categories: ages between 0 and 6 years (group I), between 7 and 12 years (group II), and between 13 and 19 years (group III). There are 26, 14 and 30 subjects in group I, II and III respectively. The main biological hypothesis of interest is if there is any localized hyoid bone growth spurts between these specific age groups.

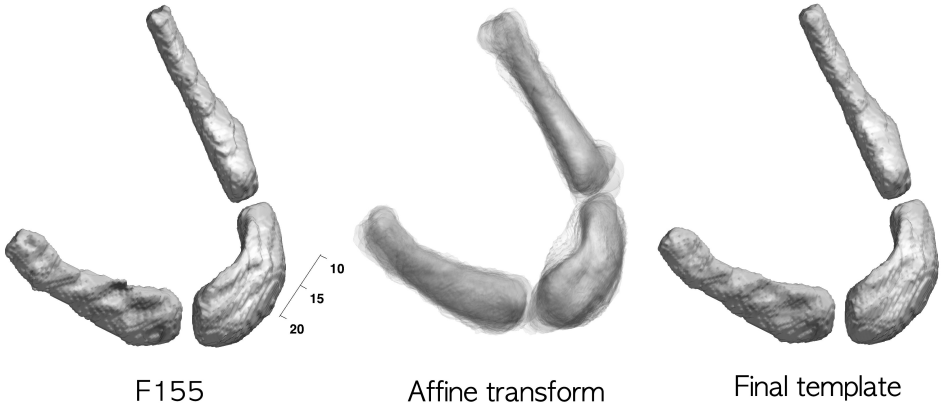

Figure 6: Left: Hyoid F155 which forms an initial template $\mathcal{M}_I$. All other mandibles are affine registered to F155. Middle: The superimposition of affine registered hyois showing local misalignments. Diffeomorphic registration is then performed to register misaligned affine transformed hyoids. Right: The average of deformation with respect to F155 provides the final population average template $\mathcal{M}_F$ where statistical parametric maps will be constructed.

4.2 Results

The displacement from the template to an individual surface is obtained at each mesh vertex. Since the length measurement provides a much easier biological interpretation, we used the length of displacement vector as a response variable among many other possible features. Since the length on the template surface is expected to be noisy due to image acquisition, segmentation and image registration errors, it is necessary perform the proposed kernel regression and subsequently reduce the type-I error and obtain more stable SPM. Figure 3 shows an example of kernel regression on our data. The kernel regression increases the signal-to-noise ratio (SNR) and improves the smoothness and Gaussianness of data. Subsequently, the heat kernel regression of the displacement length is taken as the response variable. We have chosen $t = 5$ as the bandwidth for the study since the bandwidth 5 is where the type-I error starts to flatten out in Figure 5. Note that the Fourier expansion with 500 LB-eigenfunctions is close to the original data (relative error of less than 0.3%). Hence, performing the proposed kernel regression before the statistical analysis can substantially smaller type-I error demonstrating its effectiveness.

Figure 7: Hyoid bones are binned into three age groups: group I (ages 0 and 6), group II (ages 7 and 12) and group III (ages 13 and 19) and the mean displacements between the groups are visualized. Each row shows the mean group differences of the displacement: group II - group I (first row) and group III - group II (second row). The arrows are the mean displacement differences and colors indicate their lengths in mm.

After the displacement lengths are smoothed, we constructed the F-field, or equivalently the T-field square, for testing the length difference between the age groups I and II, II and III, and I and III showing the regions of growth spurts between different age range (Figure 8). Since test statistics are constructed over all mesh vertices on the mandible, multiple comparisons were account using the random field theory [34, 38].

For testing the differences between the groups I and II, II and III, and I and III, they are based on F-field with 1 and 38, 1 and 42, and 1 and 54 degrees of freedom respectively. The result is displayed in Figure 8, where the significant results were only found between the groups II and III (middle), and I and III (bottom) at 0.1 level. Between the groups II and III, we obtained the maximum F-statistic value of 9.36 (right hyoid), which corresponds to the p-value of 0.041 (corrected). Between the groups I and III, we obtained the maximum F-statistic value of 10.55 (middle hyoid), which corresponds to the p-value of 0.028 (corrected). In the F-statistic maps for middle and bottom rows, red regions are considered as exhibiting

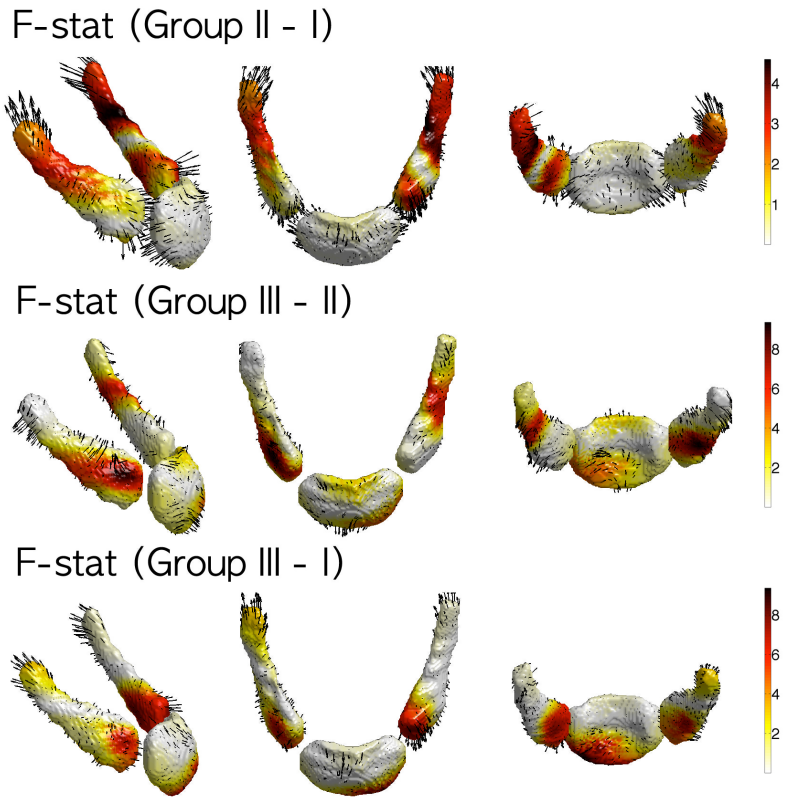

Figure 8: F-statistic maps on hyoid showing age effect between the groups. The significant growth regions (red) are identified only between group II and III, and I and III. The growth is highly localized near the regions that connect the disconnected hyoid bones.

significant growth spurts.

5 Conclusion

We have developed a new kernel regression framework on a manifold that unifies bivariate kernel regression, heat diffusion and wavelets in a single coherent mathematical framework. The kernel regression is both global and local in a sense it uses global basis functions to perform regression but locally equivalent to diffusion wavelet transform. The proposed framework is demonstrated to reduce type-I error in modeling shape variations compared

to the usual Fourier series expansion. The method is then used in developing a statistical inference procedure for functional signals on manifolds. The whole framework

Acknowledgment

This work was supported by NIH Research Grant R01 DC6282 (MRI and CT Studies of the Developing Vocal Tract), from the National Institute of Deafness and other Communicative Disorders (NIDCD); core grant P-30 HD03352 to the Waisman Center from the National Institute of Child Health and Human Development (NICHHD) and Clinical and Translational Science Award (CTSA) program, through the NIH National Center for Advancing Translational Sciences (NCATS) UL1TR000427

References

[1] R.J. Adler. *The Geometry of Random Fields*. John Wiley & Sons, 1981.

[2] A. Andrade, F. Kherif, J. Mangin, K.J. Worsley, A. Paradis, O. Simon, S. Dehaene, D. Le Bihan, and J-B. Poline. Detection of fMRI activation using cortical surface mapping. *Human Brain Mapping*, 12:79–93, 2001.

[3] J.-P. Antoine, D. Roşca, and P. Vandergheynst. Wavelet transform on manifolds: old and new approaches. *Applied and Computational Harmonic Analysis*, 28:189–202, 2010.

[4] B.B. Avants, C.L. Epstein, M. Grossman, and J.C. Gee. Symmetric diffeomorphic image registration with cross-correlation: Evaluating automated labeling of elderly and neurodegenerative brain. *Medical Image Analysis*, 12:26–41, 2008.

[5] M. Belkin and P. Niyogi. Laplacian eigenmaps and spectral techniques for embedding and clustering. In *Advances in Neural Information Processing Systems*, pages 585–592, 2002.

[6] Mikhail Belkin, Partha Niyogi, and Vikas Sindhwani. Manifold regularization: A geometric framework for learning from labeled and unlabeled examples. *The Journal of Machine Learning Research*, 7:2399–2434, 2006.

[7] J. Bernal-Rusiel, M. Atienza, and J. Cantero. Detection of focal changes in human cortical thickness: spherical wavelets versus gaussian smoothing. *NeuroImage*, 41:1278–1292, 2008.

[8] M.K. Chung, K.M. Dalton, L. Shen, A.C. Evans, and R.J. Davidson. Weighted Fourier representation and its application to quantifying the amount of gray matter. *IEEE Transactions on Medical Imaging*, 26:566–581, 2007.

[9] M.K. Chung, R. Hartley, K.M. Dalton, and R.J. Davidson. Encoding cortical surface by spherical harmonics. *Statistica Sinica*, 18:1269–1291, 2008.

[10] M.K. Chung, S. Robbins, K.M. Dalton, R.J. Davidson, A.L. Alexander, and A.C. Evans. Cortical thickness analysis in autism with heat kernel smoothing. *NeuroImage*, 25:1256–1265, 2005.

[11] M.K. Chung, S. Robbins, and A.C. Evans. Unified statistical approach to cortical thickness analysis. *Information Processing in Medical Imaging (IPMI), Lecture Notes in Computer Science*, 3565:627–638, 2005.

[12] M.K. Chung, K.J. Worsley, S. Robbins, and A.C. Evans. Tensor-based brain surface modeling and analysis. In *IEEE Conference on Computer Vision and Pattern Recognition (CVPR)*, volume I, pages 467–473, 2003.

[13] M.K. Chung, K.J. Worsley, S. Robbins, T. Paus, J. Taylor, J.N. Giedd, J.L. Rapoport, and A.C. Evans. Deformation-based surface morphometry applied to gray matter deformation. *NeuroImage*, 18:198–213, 2003.

[14] J.B. Conway. *A Course in Functional Analysis*. Springer, 1990.

[15] J. Fan and I. Gijbels. *Local Polynomial Modelling and Its Applications*. Chapman & Hall/CRC, 1996.

[16] A. Gelb. The resolution of the gibbs phenomenon for spherical harmonics. *Mathematics of Computation*, 66:699–717, 1997.

[17] D.K. Hammond, P. Vandergheynst, and R. Gribonval. Wavelets on graphs via spectral graph theory. *Applied and Computational Harmonic Analysis*, 30:129–150, 2011.

[18] S. Hayasaka, A.M. Peiffer, C.E. Hugenschmidt, and P.J. Laurienti. Power and sample size calculation for neuroimaging studies by noncentral random field theory. *NeuroImage*, 37:721–730, 2007.

[19] W.H. Kim, D. Pachauri, C. Hatt, M.K. Chung, S. Johnson, and V. Singh. Wavelet based multi-scale shape features on arbitrary surfaces for cortical thickness discrimination. In *Advances in Neural Information Processing Systems*, pages 1250–1258, 2012.

[20] J. P. Lerch and A.C. Evans. Cortical thickness analysis examined through power analysis and a population simulation. *NeuroImage*, 24:163–173, 2005.

[21] W.E. Lorensen and H.E. Cline. Marching cubes: A high resolution 3D surface construction algorithm. In *Proceedings of the 14th Annual Conference on Computer Graphics and Interactive Techniques*, pages 163–169, 1987.

[22] R Malladi and I. Ravve. Fast difference schemes for edge enhancing Beltrami flow. In *Proceedings of Computer Vision-ECCV, Lecture Notes in Computer Science (LNCS)*, volume 2350, pages 343–357, 2002.

[23] D. Nain, M. Styner, M. Niethammer, J.J. Levitt, M.E. Shenton, G. Gerig, A. Bobick, and A. Tannenbaum. Statistical shape analysis of brain structures using spherical wavelets. In *IEEE Symposium on Biomedical Imaging ISBI*, 2007.

[24] A.C. Öztireli, G. Guennebaud, and M. Gross. Feature preserving point set surfaces based on non-linear kernel regression. In *Computer Graphics Forum*, volume 28, pages 493–501, 2009.

[25] P. Perona and J. Malik. Scale-space and edge detection using anisotropic diffusion. *IEEE Trans. Pattern Analysis and Machine Intelligence*, 12:629–639, 1990.

[26] A. Qiu, D. Bitouk, and M.I. Miller. Smooth functional and structural maps on the neocortex via orthonormal bases of the laplace-beltrami operator. *IEEE Transactions on Medical Imaging*, 25:1296–1396, 2006.

[27] A. Qiu and M.I. Miller. Multi-structure network shape analysis via normal surface momentum maps. *NeuroImage*, 42:1430–1438, 2008.

[28] N. Sochen, R. Kimmel, and R. Malladi. A general framework for low level vision. *IEEE Transactions on Image Processing*, 7:310–318, 1998.

[29] B. Tang, G. Sapiro, and V. Caselles. Direction diffusion. In *The Proceedings of the Seventh IEEE International Conference on Computer Vision*, pages 2:1245–1252, 1999.

[30] G. Taubin. Geometric Signal Processing on Polygonal Meshes. In *EUROGRAPHICS*, 2000.

[31] J.E. Taylor and K.J. Worsley. Detecting sparse signals in random fields, with an application to brain mapping. *Journal of the American Statistical Association*, 102:913–928, 2007.

[32] H.K. Vorperian, S. Wang, E.M. Schimek, R.B. Durtschi, R.D. Kent, L.R. Gentry, and M.K. Chung. Developmental sexual dimorphism of the oral and pharyngeal portions of the vocal tract: an imaging study. *Journal of Speech, Language and Hearing Research*, 54:995–1010, 2011.

[33] Y. Wang, J. Zhang, B. Gutman, T.F. Chan, J.T. Becker, H.J. Aizenstein, O.L. Lopez, R.J. Tamburo, A.W. Toga, and P.M. Thompson. Multivariate tensor-based morphometry on surfaces: Application to mapping ventricular abnormalities in HIV/AIDS. *NeuroImage*, 49:2141–2157, 2010.

[34] K.J. Worlsey, J-B. Poline, A.C. Vandal, and K.J. Friston. Test for distributed, non-focal brain activations. *NeuroImage*, 2:173–181, 1995.

[35] K.J. Worsley. Detecting activation in fMRI data. *Statistical Methods in Medical Research.*, 12:401–418, 2003.

[36] K.J. Worsley, J. Cao, T. Paus, M. Petrides, and A.C. Evans. Applications of random field theory to functional connectivity. *Human Brain Mapping*, 6:364–7, 1998.

[37] K.J. Worsley, S. Marrett, P. Neelin, A.C. Vandal, K.J. Friston, and A.C. Evans. A unified statistical approach for determining significant signals in images of cerebral activation. *Human Brain Mapping*, 4:58–73, 1996.

[38] K.J. Worsley, J.E. Taylor, F. Tomaiuolo, and J. Lerch. Unified univariate and multivariate random field theory. *NeuroImage*, 23:S189–195, 2004.

[39] Y. Xu, D.J. Valentino, A.I. Scher, I. Dinov, L.R. White, P.M. Thompson, L.J. Launer, and A.W. Toga. Age effects on hippocampal structural changes in old men: the haas. *NeuroImage*, 40:1003–1015, 2008.

[40] P.A. Yushkevich, H. Zhang, T.J. Simon, and J.C. Gee. Structure-specific statistical mapping of white matter tracts. *NeuroImage*, 41:448–461, 2008.

[41] H. Zhang, O. van Kaick, and R. Dyer. Spectral methods for mesh processing and analysis. In *EUROGRAPHICS*, pages 1–22, 2007.

Appendix

Theorem 1

$$\widehat{h}(p) = \arg\min_{h \in \mathcal{H}_k} \int_{\mathcal{M}} \int_{\mathcal{M}} K(p,q) \Big| f(q) - h(p) \Big|^2 \, d\mu(q) \, d\mu(p) = \sum_{j=0}^{k} \tau_j f_j \psi_j.$$

Proof. Any function $h \in \mathcal{H}_k$ can be expressed as

$$h(p) = \sum_{j=0}^{k} \beta_j \psi_j(p). \tag{12}$$

Then by plugging (12) into the inner integral $I(p)$, it becomes

$$I(p) = \int_{\mathcal{M}} K(p,q) \Big| f(q) - \sum_{j=0}^{k} \beta_j \psi(p) \Big|^2 \, d\mu(q).$$

Simplifying the expression, we obtain

$$I(p) = \sum_{j=0}^{k} \sum_{j'=0}^{k} \psi_j(p) \psi_{j'}(p) \beta_j \beta_{j'} - 2K * f(p) \sum_{j=0}^{k} \psi_j(p) \beta_j + K * f^2(p). \tag{13}$$

From Mercer's theorem [14], the kernel can be written as

$$K(p,q) = \sum_{j'=0}^{\infty} \tau_{j'} \psi_{j'}(p) \psi_{j'}(q). \tag{14}$$

The convolution is then written as

$$K * f(p) = \sum_{j'=0}^{\infty} \tau_{j'} f_{j'} \psi_{j'}(p).$$

Since I is an unconstrained positive semidefinite quadratic program (QP) in β_j, there is no unique global minimizer of I without additional linear constraints. Integrating I further with respect to $d\mu(p)$, we collapses (13) to a positive definite QP, which yields a unique global minimizer:

$$\int_{\mathcal{M}} I(p) \, d\mu(p) = \sum_{j=0}^{k} \beta_j^2 - 2 \sum_{j=0}^{k} \tau_j f_j \beta_j + \text{ const.}$$

The minimum of the above integral is obtained when all the partial derivatives with respect to β_j vanish, i.e.

$$\int_{\mathcal{M}} \frac{\partial I}{\partial \beta_j}\, d\mu(p) = 2\beta_j - 2\tau_j f_j = 0$$

for all j. Hence $\sum_{j=0}^{k} \tau_j f_j \psi_j$ must be the unique minimizer. $\square$

Theorem 2. For an arbitrary self-adjoint differential operator $\mathcal{L}$, the unique solution of the Cauchy problem

$$\frac{\partial g(p,t)}{\partial t} + \mathcal{L}g(p,t) = 0, g(p,t=0) = f(p) \tag{15}$$

is given by

$$g(p,t) = \sum_{j=0}^{\infty} \tau_j f_j \psi_j(p) \;\text{ with }\; \tau_j = e^{-\lambda_j t}. \tag{16}$$

Proof. For each fixed t, $g(p,t)$ can be written as

$$g(p,t) = \sum_{j=0}^{\infty} c_j(t)\psi_j(p). \tag{17}$$

Then

$$\mathcal{L}g(p,t) = \sum_{j=0}^{\infty} c_j(t)\lambda_j\psi_j(p). \tag{18}$$

Substituting (17) and (18) into (8), we obtain

$$\frac{\partial c_j(t)}{\partial t} + \lambda_j c_j(t) = 0 \tag{19}$$

for all j. The solution of equation (19) is given by $c_j(t) = b_j e^{-\lambda_j t}$. So we have a solution

$$g(p,t) = \sum_{j=0}^{\infty} b_j e^{-\lambda_j t}\psi_j(p).$$

At $t = 0$, we have

$$g(p,0) = \sum_{j=0}^{\infty} b_j \psi_j(p) = f(p).$$

The coefficients b_j must be the Fourier coefficients, i.e.

$$b_j = \langle f, \psi_j \rangle = f_j. \square$$

Theorem 3. The statistical power $\mathcal{P}$ of testing the hypotheses

$$H_0 : h(p) = 0 \text{ for all } p \in \mathcal{M} \text{ vs. } H_1 : h(p) = c\sigma > 0 \text{ for some } p \in \mathcal{M}.$$

using the T random field $T(p)$ is given by

$$\mathcal{P}(n) \approx 1 - \exp\Big[- \sum_{j=0}^{d} \mu_j(\mathcal{M}_1)\rho_j(t_\alpha^* - c\sqrt{n})\Big],$$

where t_α^* is the α-quantile given by

$$\alpha = P\Big(\sup_{p \in \mathcal{M}} T(p) > t_\alpha^* \Big).$$

Proof. In the region $\mathcal{M}_0$ corresponding to H_0,

$$f^i(p) \sim N(0, \sigma^2).$$

In the region $\mathcal{M}_1$ corresponding to H_1,

$$f^i(p) \sim N(c\sigma, \sigma^2).$$

Figure 9 illustrates this setting.

Consider the test statistic

$$T(p) = \frac{\bar{f}(p)}{S(p)/\sqrt{n}}, \tag{20}$$

where $\bar{f}$ and S are the sample mean and standard deviation of the measurements $f^i, \cdots, f^n$. In $\mathcal{M}_0$, $T(p)$ is a T random field with $n-1$ degrees of freedom [1]. In $\mathcal{M}_1$, $T(p)$ can be written as

$$T(p) = T'(p) + \frac{c\sigma}{S(p)/\sqrt{n}},$$

where $T'(p)$ a T random field with $n-1$ degrees of freedom. Since σ is usually estimated using the standard deviation, approximately we have $S(p) = \sigma$ and the test statistic becomes

$$T(p) = T'(p) + c\sqrt{n}.$$

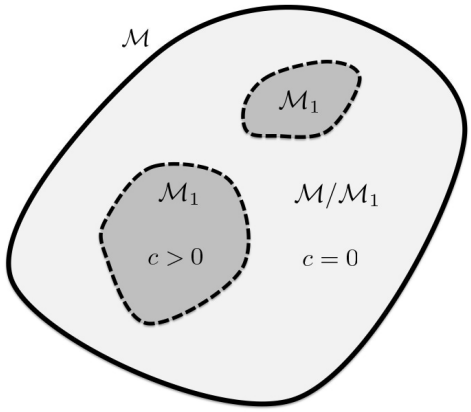

Figure 9: Schematic of when H_1 is true.

At each fixed p, $T(p)$ is no longer a T random field but a non-central T random field [18]. Subsequently the power $\mathcal{P}$ at the given α-level is given by

$$\begin{aligned} \mathcal{P}(n) &= P\Big(\sup_{p\in\mathcal{M}_1} T(p) > t^*_\alpha\Big) && (21)\\ &= P\Big(\sup_{p\in\mathcal{M}_1} T'(p) > t^*_\alpha - c\sqrt{n}\Big), && (22)\end{aligned}$$

where t^*_α is the α-quantile of $\sup_{p\in\mathcal{M}} T(p)$ under H_0, i.e.

$$\alpha = P\Big(\sup_{p\in\mathcal{M}} T(p) > t^*_\alpha\Big).$$

Although (21) is intractable to directly compute, we will approximate (22) using the expected Euler characteristic (EC) method [37, 35]. The power (22) can be written as

$$\mathcal{P}(n) = \sum_{j=0}^{d} \mu_j(\mathcal{M}_1)\rho_j(t^*_\alpha - c\sqrt{n}),$$

where $\mu_d(\mathcal{M})$ is the j-th Minkowski functional or intrinsic volume of $\mathcal{M}$ and ρ_j is the j-th EC-density of T-field [36, 1, 31, 35]. The expansion only works for sufficiently large $t^*_\alpha - c\sqrt{n}$. For small threshold, the power may not be bounded between 0 and 1. So it is necessary to use the exponential transform used in [18] to bound the power. For small $\mathcal{P}(n)$, using the Taylor

expansion, we can write

$$\exp\big[-\mathcal{P}(n)\big] \approx 1 - \mathcal{P}(n).$$

Equivalently, it is written as

$$\mathcal{P}(n) \approx 1 - \exp\big[-\mathcal{P}(n)\big].$$

This transformation guarantees the power estimation to be bound between 0 and 1 [18]. Subsequently, the power is given by

$$\mathcal{P}(n) = 1 - \exp\Big[-\sum_{j=0}^{d} \mu_j(\mathcal{M}_1)\rho_j(t^*_\alpha - c\sqrt{n})\Big].\square$$